Volume 27
Number 46
14 December 2025
Pages 14735-14966

Green Chemistry

Cutting-edge research for a greener sustainable future

rsc.li/greenchem

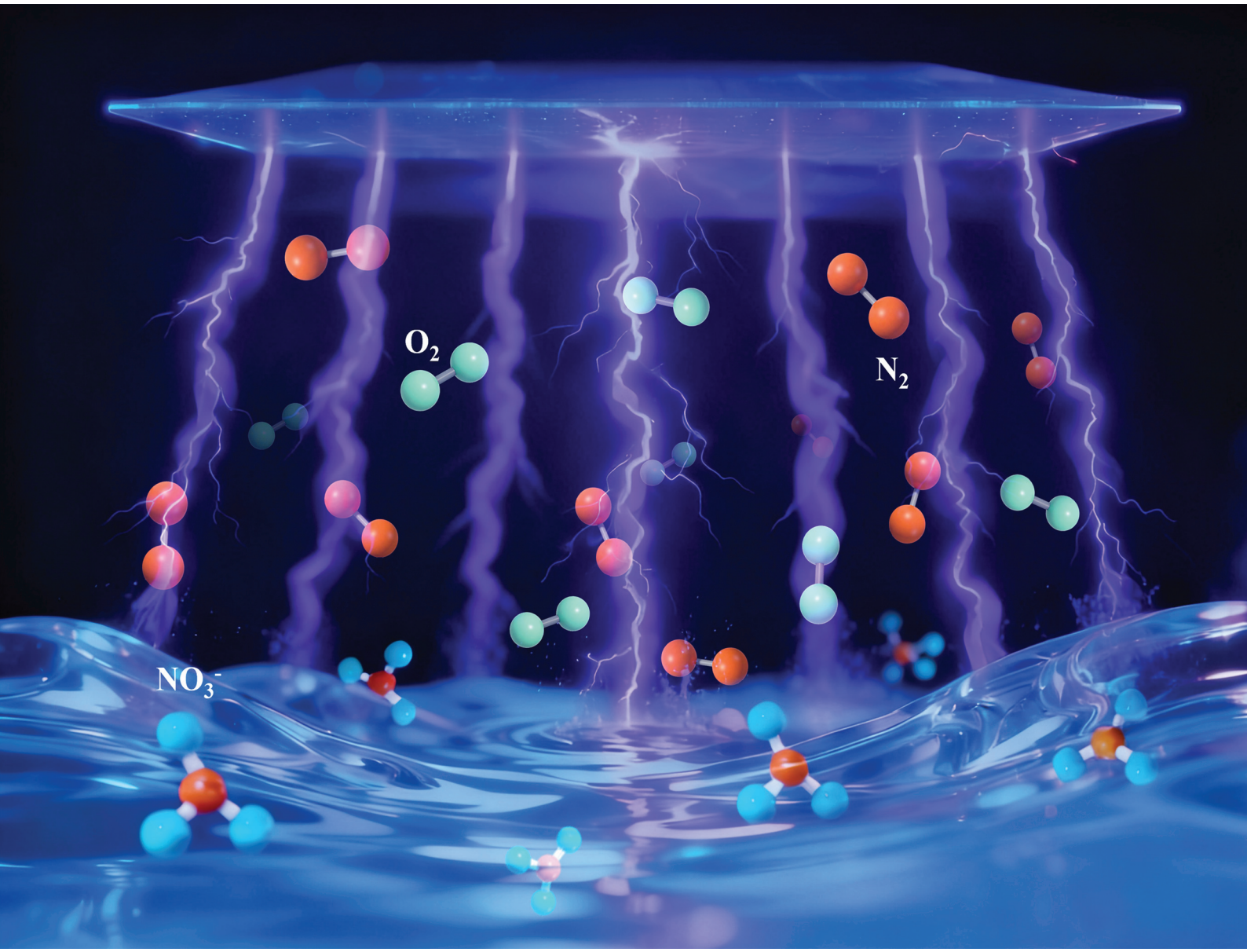

ISSN 1463-9262

ROYAL SOCIETY OF CHEMISTRY

PAPER

Su-Rong Sun *et al.*

Enhanced nitrogen fixation using DBD plasma with continuous flowing water and a TiO_2 photocatalyst coupled system

25 YEARS ANNIVERSARY

Green Chemistry

PAPER

Cite this: *Green Chem.*, 2025, **27**, 14807

Enhanced nitrogen fixation using DBD plasma with continuous flowing water and a TiO_2 photocatalyst coupled system

Wen-Dong Wan,[a] Su-Rong Sun, *[a] Chao Wang,[a] Yury Gorbanev, [b] Hai-Xing Wang[a,c] and Annemie Bogaerts [b]

Received 2nd May 2025,
Accepted 9th September 2025

DOI: 10.1039/d5gc02201k

rsc.li/greenchem

In this study, a novel dielectric barrier discharge (DBD) with continuous flowing water is designed (other devices commonly utilize immobile water), which could be easily coupled with UV light and TiO_2 to achieve highly efficient nitrogen fixation (NF) from air plasma over water surface. Electrical characterization, optical emission spectroscopy and X-ray photoelectron spectroscopy (XPS) are performed to study the plasma properties and underlying mechanisms of NF under different conditions. Results indicate that the maximum nitrate concentration and minimum energy consumption can reach 154 mg L^{-1} and 61 MJ mol^{-1}, respectively, in the case of pure plasma. The total amount of dissolved nitrogen (TN) reaches a maximum concentration of 199 mg L^{-1}, indicating that the main nitrogen fixation product is nitrate, while the nitrite concentration is very low. By coupling TiO_2 spheres in the water and UV light, the concentration of nitrate and TN increases by 57% and 45%, respectively, compared with the pure plasma condition at an input power of 200 W and a processing time of 20 min. XPS analysis directly demonstrates a change in the Ti valence state on the TiO_2 surface, indicating the formation of more electron–hole pairs. Thus, more highly oxidizing species are formed on the photocatalyst surface to enhance the production of NO_x. A mechanism is proposed that describes the underlying chemistry in the gas and liquid phases and the enhanced NF efficiency upon the addition of TiO_2 spheres and UV light irradiation. As the use of the circulating water as the ground electrode can lead to thermal quenching, the novel DBD NF device can realize continuous operation time at a relatively high power, offering good application prospect.

Green foundation

1. This study presents a novel green nitrogen fixation method by designing a dielectric barrier discharge (DBD) system using continuous flowing water as the ground electrode, which is further coupled with UV light and TiO_2 to achieve highly efficient nitrogen fixation (NF) from air plasma over the water surface.
2. The maximum concentration and production rate are 154 mg L^{-1} and 162 μmol min^{-1}, respectively, at an input power of 200 W under pure DBD plasma. Compared with the case of pure plasma, adding TiO_2 and UV irradiation results in a significant rise in the NO_3^- concentration and production rate by 57% and 37%, respectively, and a drop in the energy cost (EC) by 28%.
3. This novel DBD NF device has a large discharge area and can work for extended periods of time at a relatively high power with no observed heat damage to the reactor, thereby offering good application prospects.

1. Introduction

Sustainable nitrogen fixation (NF) technology has received extensive attention from researchers worldwide due to the high energy cost and emission of greenhouse gases into the atmosphere by the Haber–Bosch (H–B) process, which consumes 1%–2% of the world's energy production and 3%–5% of the total annual natural gas production[1–4] and emits more than 300 million tons of carbon dioxide gas.[5,6] In a low-temperature plasma environment, the otherwise highly unreactive N≡ triple bond of N_2 molecules can be "broken" *via* direct electron impact reactions with plasma electrons and through collisions with highly reactive species. This makes the use of plasma a promising NF method, with the theoretical energy consumption (EC) limit claimed to be as low as 0.2 MJ mol^{-1}.[7] However, this estimate is based on strong vibrational-translational nonequilibrium conditions, which are difficult to achieve, and hence, this low value has not been experimentally

[a]*School of Astronautics, Beihang University, 100191 Beijing, China. E-mail: ssr18@buaa.edu.cn*
[b]*Research group PLASMANT, Department of Chemistry, University of Antwerp, 2610 Antwerp, Belgium*
[c]*Ningbo Institute of Technology, Beihang University, 315800 Ningbo, China*

demonstrated to date. In 1903, a thermal electric arc was used to convert N_2 into NO_x,[8,9] but in thermal plasmas, most of the energy is directed towards heating the gas, which leads to a lower energy efficiency. Interestingly, low-temperature plasmas are more energy-efficient as they enable non-thermodynamically limited reactions.[7] Thus, non-thermal plasma has gained increased interest because it can produce NO_x at room temperature and atmospheric pressure.[5,10]

Currently, a variety of non-thermal as well as warm (*i.e.*, quasi-thermal) plasma sources have been used for NF, including dielectric barrier discharge (DBD),[11–14] transient spark discharge,[15–17] gliding arc,[18–23] microwave plasma[24] and pin-to-pin low-current arc.[25] The NF products of most non-thermal or warm plasma sources are gaseous NO_x, which cannot be directly used and need to be converted into NO_x^-. Thus, the use of plasma–water interaction systems to produce NO_x^-, which can be used directly in agricultural production, has attracted wide attention.[26,27] Plasma–water NF systems typically operate in air plasma at atmospheric pressure, with EC and NO_x^- concentrations in the range of 15–700 MJ mol^{-1} and 1–900 mg L^{-1}, respectively.[2,17,19,28] The lowest EC for NF in water using an arc-DBD combination reached 8 MJ mol^{-1} with a NO_x^- concentration of 141 mg L^{-1}, for a plasma reactor power of 160 W and 95 W supplied power of an ozone generator;[29] however, since extra O_3 was introduced into the mixing chamber through an ozone generator to promote oxidation of the gas phase substrates and transition products, this also increased the complexity of the device. Spark discharge and gliding arc plasma in contact with water are also commonly used for NF, due to the simplicity of such devices; however, because of the limited discharge volumes in these two types of discharge devices, only small amounts of gas are typically treated, which reduces the NF yield. Gorbanev *et al.* achieved a low EC of 15 MJ mol^{-1} using pulsed spark plasma, with the highest total concentration of NH_3 and NO_2^-/NO_3^- of about 21 mg L^{-1}, but their device had only 0.11 W of power and treated only 5 mL of water.[2] Generally, current plasma–water-based NF systems still face several challenges that need to be addressed, such as low yields, complex device architectures, limited water treatment volumes and short working times, which limit the development and application of such NF systems.

In response to the above issues, NF studies in plasma–water interaction systems, coupled with other technologies, for example, ultraviolet (UV) light sources,[28,30,31] titanium dioxide (TiO_2) catalysts[32] or a combination of UV and TiO_2,[33] have been gaining interest from both the scientific community and industry. Peng *et al.* pointed out that irradiating the water surface with UV light can promote the excitation of water molecules, leading to an increase in NO_3^- synthesis rate from 29 μmol min^{-1} without UV to 61 μmol min^{-1} with UV.[31] Sun *et al.* adopted a DBD discharge reactor coupled with TiO_2 catalyst to achieve 93% selectivity for NO_3^-, but the total NO_x^- concentration and EC were about 33 mg L^{-1} and 50 MJ mol^{-1}, respectively.[32] Thus, there is still much room for improvement in the plasma and UV/TiO_2 coupled system. Moreover, systematic research on the application of TiO_2 combined with UV light to produce NO_3^- is virtually non-existent. Therefore, it is worth conducting in-depth research on the combined effect of TiO_2 and UV light on NF performance, since it is expected to have a positive impact on the production of NO_x in plasma–water interaction systems.

Previous studies on DBD nitrogen fixation usually adopted the typical "pin-plate" reactor[2] or "plate-plate" structure,[14] which both achieve low effective reaction areas of <5 cm^2 with a liquid volume of <20 mL, severely constraining nitrogen fixation efficiency and scalability. Furthermore, liquid evaporation in static systems may destabilize the gas–liquid interface and hinder sustained operation. Therefore, in this work, we designed a novel DBD reactor utilizing continuously flowing water as the ground electrode, overcoming the two limitations observed in most DBD nitrogen fixation systems; *i.e.*, confined reaction area and gas–liquid interface instability. In our setup, a large quartz plate serves as the dielectric barrier with a circular metal electrode (high-voltage) positioned on the quartz, with a grounded copper line inserted in the flowing water. Thus, the DBD reactor can achieve an effective reaction area of 33 cm^2 with a treated water volume of 2 L. The system can work for extended periods at relatively high power, with a stable gas–liquid interface due to the reduced temperature caused by the flowing water. Details of the DBD reactor and the experimental system are presented in Section 2. Electrical characterizations with a digital oscilloscope, as well as UV-vis spectrophotometry and spectroscopic diagnostics, were collected and used to investigate the plasma properties and determine nitrogen oxide concentrations. In Section 3, the plasma properties, product concentrations and underlying NF mechanisms are analyzed under pure plasma, plasma + UV, plasma + TiO_2, and plasma + UV + TiO_2 conditions. The product concentrations and EC are analyzed at different input powers and treatment times and compared with previously reported NF results. Finally, the results are discussed in the conclusion (Section 4).

2. Materials and methods

2.1 Experimental setup

Fig. 1 presents the DBD experimental system used for NF, as well as the frontal and lateral discharge images. The DBD reactor consists of a quartz container with a height of 36 mm and an inner diameter of 140 mm, a polytetrafluoroethylene (PTFE) cover plate, a stainless-steel mesh, a copper line and a quartz dielectric plate. The PTFE cover plate (diameter 180 mm and thickness 5 mm) and the stainless-steel mesh (diameter 65 mm) are placed on the central region of the PTFE cover plate. The circular quartz dielectric plate (diameter 100 mm and thickness 2 mm) is located below the stainless-steel mesh. A copper line with a diameter of 3 mm is grounded and inserted into the quartz container from the bottom. In this way, deionized (DI) water in the quartz container with a volume of 550 mL is connected to the ground electrode. The

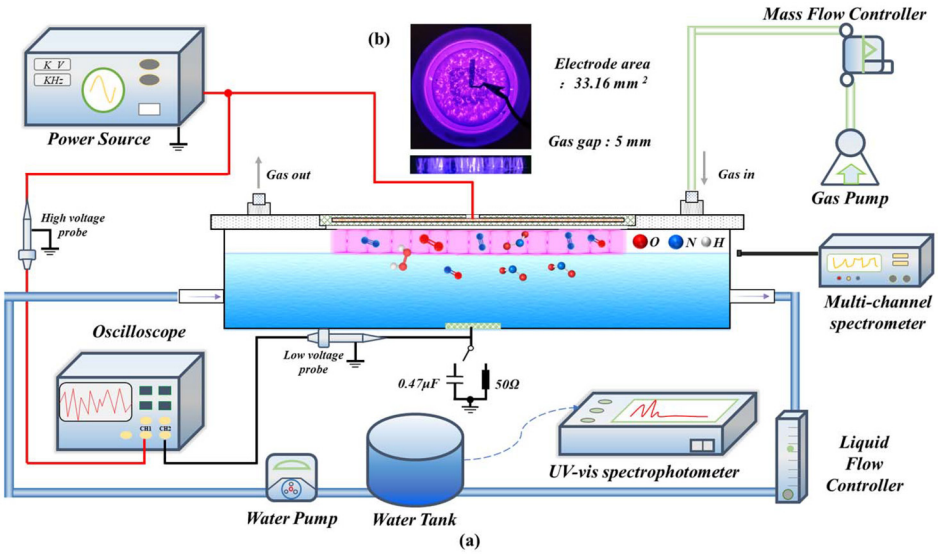

Fig. 1 Schematic of the experimental setup (a), and frontal and lateral discharge images (b).

discharge gap between the quartz dielectric and the water surface is set to 5 mm. Air is supplied to the reactor by an air compressor and the air flow rate is adjusted with a mass flow controller. Water circulation between the discharge reactor and water tank is performed with a water pump, and a liquid regulating valve is used to control the water flow velocity and maintain the stability of the water surface. The volume of water in the water tank is 2 L, and the water flow rate is kept at 200 mL min^{-1}. As pointed out in ref. 34, using a reactor with static liquid can have diffusion-related limitations, such as accumulation of the products in the upper layer of the liquid. Therefore, our gaseous plasma in contact with flowing liquid has the advantage of reducing the accumulation of heat and active species, which is expected to improve the NF product concentration.

At the gas–liquid interface and within the liquid phase, the temperature is measured using K-type thermocouples with a thermocouple thermometer (HT-9815). The discharge reactor is powered by a high-voltage alternating current (AC) power supply (Nanjing Suman Plasma Technology Co., Ltd, CTP-2000 K). The input power of the power supply is adjusted to change the NF process. The discharge voltage and current are measured by high-voltage (Tektronix, P6015A) and low-voltage (Tektronix, P2220) probes, respectively, which are connected to a four-channel digital oscilloscope (Tektronix, MDO3034).

2.2 Experimental design

In the experiments, the power, air flow rate and treatment time were adjusted to study their effects on the pH and the concentrations of NO_3^- and total nitrogen (TN; *i.e.*, the sum of all dissolved nitrogen, including the concentrations of NO_2^-, NO_3^- and NH_4^+). However, in air DBD plasma–water systems, the amount of NH_3/NH_4^+ produced is negligible;[35] thus, the NH_4^+ concentrations were not separately measured in this work. Since the water in contact with the plasma was flowing and hence provided cooling of the system, the input power can reach a high level of 200 W in our study (which is significantly higher than in most works, which use power levels of <100 W) without introducing thermal damage to the system, and we expect that this high input power facilitates the NF.

Specifically, we varied the power from 75 to 200 W with an increment of 25 W while maintaining an output frequency of about 9 kHz. The air flow rate was changed from 0 to 2.5 L min^{-1} at intervals of 0.5 L min^{-1}, and the treatment time was set to 10, 20, 30 and 40 min. After the generation of plasma-activated water (PAW), the pH and the concentrations of NO_3^- and TN were immediately measured. H_2O_2 can also be formed from the recombination of OH radicals produced from water dissociation,[14,35] although we do not discuss this aspect in detail in this paper. Here, we focus on the concentrations of NO_3^- and TN, and examine their variations under different conditions.

To further improve the concentrations of nitrogen oxide species in water, we also examined the use of combinations of UV light irradiation and titanium dioxide (TiO_2) particles (2 g) submerged in the water, as shown in Fig. 2. We compared the results of the experiments using plasma alone, plasma with UV light irradiation, plasma with TiO_2 particles and plasma with UV light irradiation and TiO_2 particles. These experiments were repeated three times with treatment times of 20 min and different power levels to obtain the average concentrations of NO_3^- and TN and their associated error.

2.3 Measurement method

Immediately after each experiment, the pH was measured with a portable pH meter (Kodak, CT-6321). The concentrations of NO_3^- and TN in the water were measured using a UV-vis spectrophotometer (Beijing Puxi General Instrument Co., Ltd, TU-1901) at the maximum absorption wavelength of 210 nm

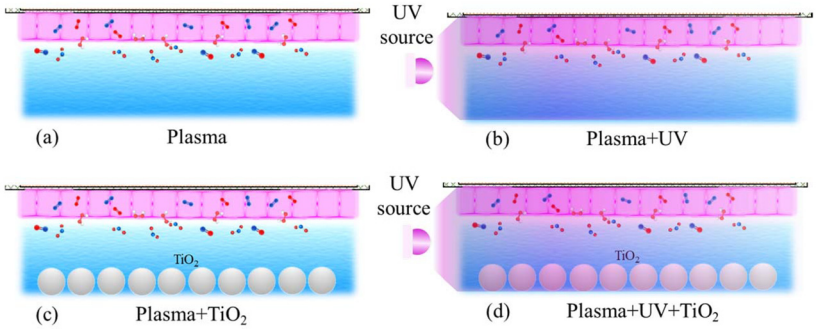

Fig. 2 Four different cases evaluated for NF.

(see SI, Section 1). We also used optical emission spectroscopy (OES) to identify the active species in the plasma, using a spectrometer (Avantes, AvaSpec-ULS4096CL) with an integration time of 3 s in the wavelength range of 300–1100 nm. An Andor iStar-intensified-sCMOS with a Zolix spectrograph was used to identify the excited species ranging from 280 to 300 nm. XPS analysis was performed using a Thermoescalab 250XI (Suzhou Science Instrument Co, LTD) to analyze the valence state of Ti on the surface of TiO_2. To assess the effectiveness of the plasma treatment, the production rate of TN and the EC were determined using eqn (1) and (2), respectively.

$$\text{Production rate}\,(\mu\text{mol min}^{-1}) = \frac{c_{\text{TN}}\,(\text{mol L}^{-1}) \times V\,(\text{L}) \times 10^{6}\,(\mu\text{mol mol}^{-1})}{t\,(\text{min})} \quad (1)$$

$$\text{EC}\,(\text{MJ mol}^{-1}) = \frac{P\,(\text{W}) \times t\,(\text{min}) \times 60\,(\text{s min}^{-1}) \times 10^{-6}\,(\text{MJ J}^{-1})}{c_{\text{TN}}\,(\text{mol L}^{-1}) \times V\,(\text{L})} \quad (2)$$

Here, c_{TN} is the measured total nitrogen concentration in the water (mol L^{-1}), V is the total water volume of the water tank, t is the processing time (min). P in eqn (2) contains the power of both the UV light and the discharge power (W). The discharge power is calculated from the discharge current and voltage as follows:

$$P = \frac{1}{T}\int_0^T U(t)I(t)\mathrm{d}t \quad (3)$$

where U represents the applied voltage, I is the discharge current, and T is a single voltage period.

3. Results and discussion

3.1 NF using only air DBD with circulating flowing water

3.1.1 Electrical properties of air plasma. Fig. 3 shows the voltage and current waveforms at different input powers and gas flow rates. The voltage basically exhibits a sinusoidal waveform with a peak value of about 15 kV, depending on the conditions. The current waveform is a superposition of a sinusoidal displacement current and a large number of micro-discharge pulses. A large number of discharge current pulses occur in the rising edge of the discharge voltage waveforms, which indicates that plenty of filamentary discharge channels are established in the gas gap during the discharge.

The maximum current pulse intensity can reach nearly 200 mA with a duration of hundreds of nanoseconds. The current pulses are reversed in the negative half of the voltage period. Moreover, the peak value of the conduction current in the negative half cycle differs from that in the positive half cycle. The asymmetry of the current pulses in the positive and negative half cycles is because the electrons in the discharge channels move towards the surface of the quartz dielectric plate in the positive half period, while the quartz dielectric surface acts as the source of electron current in the negative half period.[36]

To quantitatively describe the variation of the current pulses, we applied numerical methods from the Origin software analyzer toolbox to determine the number of micro-discharges (N_{md}), their peak intensity (I_{md}), and pulse lifetime (t_{md}).[37] As the input power increases from 75 W to 175 W, the number of micro-discharge current pulses (N_{md}) rises from 54 to 110, as illustrated in Fig. 3, and this is accompanied by an increase in the effective dielectric capacitance of the DBD reactor, as shown in Table 1. This indicates that more micro-discharge channels are generated in the gas gap, and correspondingly, the spatial plasma uniformity is improved at a larger discharge power. It can be observed from Fig. 3 that the time intervals between current pulses are shorter at higher discharge powers, which corresponds to a denser spatial distribution of discharge filaments, as shown in Fig. 4(b). The spatial evolution of the generation, development, and disappearance of discharge filaments in Fig. 4 is a macroscopic manifestation of the current pulses. At a power of 75 W (Fig. 4(a)), the plasma region flickers, the discharge filaments are not uniform, and the corresponding number of micro-discharge current pulses is very small, as shown in Fig. 3(a), which is in line with previous reports.[38] As shown in Fig. 4(b), when the power is increased to 200 W, the discharge filaments tend to be spaced more uniformly and are more stable. The durations of the current pulses within a cycle are also extended with higher power, indicating longer discharge times within

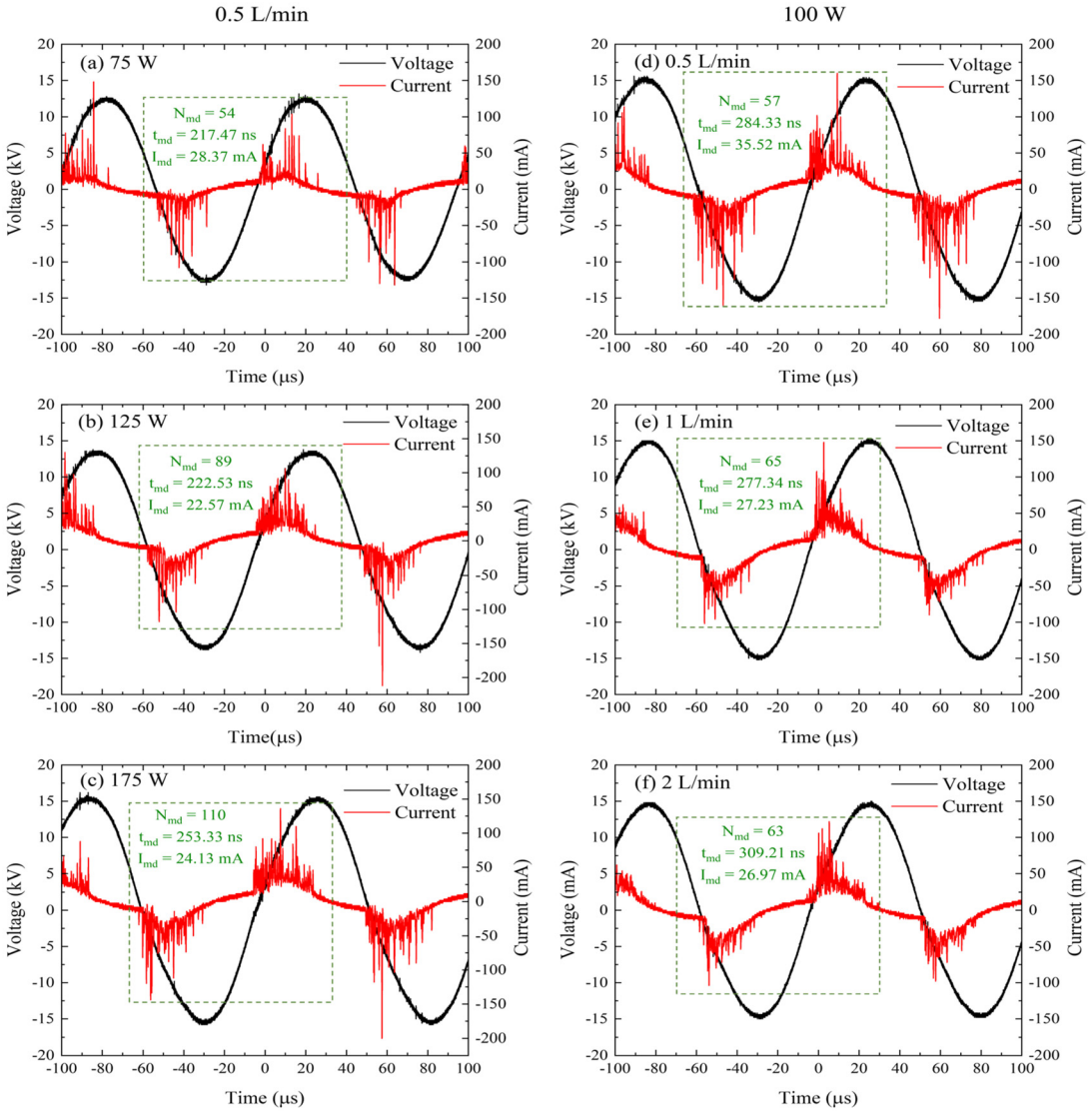

Fig. 3 Voltage and current waveforms at different input powers (a–c) with a fixed gas flow rate of 0.5 L min^{-1} and at different gas flow rates (d–f) at a fixed power of 100 W.

Table 1 Effective dielectric capacitance, maximum transferred charge, average reduced electric field and electron temperature calculated at different operating conditions (input power and air flow rate)

Input power (W)	Air flow rate (L min^{-1})	Effective dielectric capacitance (pF)	Maximum transferred charge (nC)	Average reduced electric field (Td)	Electron temperature (eV)
75	0.5	33	346	117	3.2
100	0.5	38	456	144	4
125	0.5	45	589	156	4.3
150	0.5	54	763	168	4.6
175	0.5	61	882	188	5
200	0.5	73	1123	197	5
150	1	58	841	173	4.7
150	2	57	846	170	4.6

the gas gap between the quartz dielectric and the water surface. Therefore, at higher discharge powers, the plasma tends to be spatially uniform and long-lasting, which facilitates gas conversion in the discharge filaments. Finally, as shown in Fig. 3(d)–(f), the gas flow rate has little influence on the number and average lifetime of micro-discharge current pulses, also causing also little effect on the gas conversion in the discharge filaments.

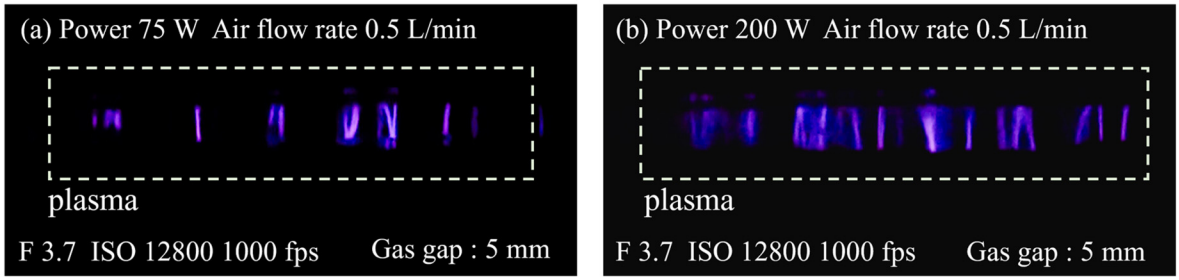

Fig. 4 Discharge images at an input power of 75 W (a) and 200 W (b) and at an air flow rate of 0.5 L min^{-1}.

To clearly elucidate the effect of different input power and gas flow rates, we calculated the effective dielectric capacitance, the maximum transferred charge per half-cycle, and the average reduced electric field, based on the Lissajous figures (see SI, Section 2);[39] the data are presented in Table 1. The electron temperature is obtained from the reduced electric field, using Bolsig+.[40] As the input power rises from 75 W to 200 W, the effective dielectric capacitance gradually increases from 33 pF to 73 pF, indicating that the area of the non-discharge region drops with input power, resulting in an increase in the transferred charge per half cycle from 346 nC to 1123 nC. The transferred charge is closely related to the electron number density in the micro-discharge channels in a DBD reactor, indicating that more electrons are present and involved in the chemical kinetic processes.

The reduced electric field and electron temperature exhibit a significant increase with rising input power, while they remain almost constant with variation of gas flow rate. Higher powers yield higher electric fields and thus higher electron temperatures. In the power range from 75 W to 200 W, the average reduced electric field and average electron temperature are enhanced from 117 Td to 197 Td and from 3.2 eV to 5.2 eV, respectively. Higher electric fields, and thus electron temperatures, are typically beneficial for electron impact excitation, dissociation and ionization reactions, possibly leading to increased production of NO_x in the plasma discharge region (if electron impact processes are dominant, which is typically the case in DBD plasmas), and thus promoting the synthesis of NO_3^- and TN in the liquid phase. This will be discussed further in Section 3.1.3.

3.1.2 Optical properties of air plasma. Besides the electrons, the radicals and excited species also play a critical role in the production of NO_x; therefore, we performed OES to investigate the changes in the emission intensity of excited species. Fig. 5 shows the measured emission spectrum at an air flow rate of 0.5 L min^{-1} and input power of 200 W. It is clear that the second positive system of N_2 ($C^3\Pi_u$-$B^3\Pi_g$, SPS) is dominant in the emission spectrum. In addition, the first negative system of N_2^+ ($B^2\Sigma_u^+$-$X^2\Pi_g^+$, FNS), the de-excitation of OH ($A^2\Sigma^+$-$X^2\Pi$) and of O atoms (O I), the first positive system of N_2 ($B^3\Pi_g$-$A^3\Sigma_u^+$, FPS) and NO ($A^2\Sigma^+$-$X^2\Pi$) can also be observed. This suggests that excited species are also likely to contribute to the formation of NO_x, either directly from N_2(C), N_2(A) and O, or indirectly through OH radical (instead or together with O) production, and these plasma reactive species then transfer to the liquid phase to induce secondary reactions, generating aqueous species, such as NO_2^- and NO_3^-.[41]

Based on the OES data, we determined the important plasma parameters, T_{vib} and T_{rot}, using the Specair software[42] (see SI, Section 3), as shown in Fig. 6. Note that the vibrational temperature T_{vib} is determined from the OES data and is thus related to the electronically excited levels of N_2. There is no evidence that this higher vibrational temperature also induces enhanced vibrational dissociation of N_2. T_{rot} is a measure of the gas temperature in the plasma. In the power range from 75 W to 200 W, T_{rot} rises from 600 K to 920 K, and T_{vib} increases from 3650 K to 4250 K. The variation of T_{rot} and T_{vib} as a function of input power is consistent with previously reported results.[43] Overall, T_{rot} is much lower than T_{vib}, which means there is obvious vibrational-rotational non-equilibrium. The low rotational temperature means that little energy is consumed to generate Joule heating, *i.e.*, thermal decomposition of species by heating is limited. Higher input powers lead to increased T_{rot}, which can also elevate the temperature of the liquid phase. However, in our setup, the water circulation system prevents the temperature of the liquid phase from rising too high, enabling the discharge reactor to work continuously for extended periods at a high power of 200 W.

3.1.3 NO_3^- and TN concentrations in the liquid phase. Fig. 7 shows the variations of NO_3^-, TN concentrations, and energy consumption with air flow rate at an input power of 150 W. When the gas flow rate increases from 0.5 L min^{-1} to 2.5 L min^{-1}, the NO_3^- concentrations are maintained at about 100–110 mg L^{-1}. As shown in Table 1, when the gas flow rate increases, there is no obvious change in electron temperature, which is consistent with the results in literature.[43] Given that electron temperature is a key factor influencing reaction kinetics, thus the change of electron-involved chemical reactions is very little, leading to the weak variation in product concentrations. TN concentration first slightly increases and then decreases, with a maximum of 141 mg L^{-1} at a gas flow rate of 1 L min^{-1}. The energy consumption also increases from 63 MJ mol^{-1} to 76 MJ mol^{-1} with the increase in gas flow rate. This is because the specific energy input and residence time of the reactants in the gas phase decrease with increasing gas flow rate, which can reduce the NF efficiency.

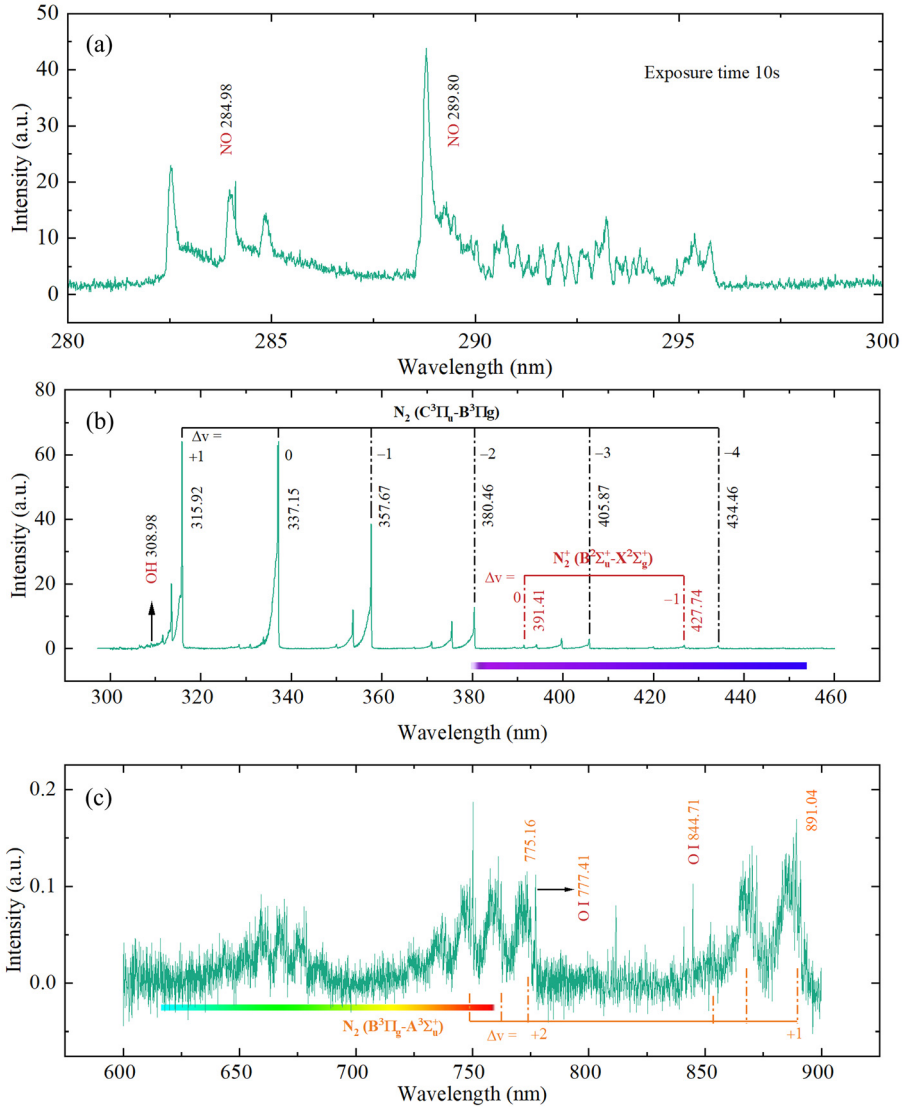

Fig. 5 Measured emission spectrum at an air flow rate of 0.5 L min^{-1} and an input power of 200 W in 280–300 nm (a), 300–460 nm (b) and 600–900 nm (c) wavelength region.

Fig. 8 presents the variation of NO_3^- and TN concentrations with input power, for various treatment times. The concentrations of NO_3^- and TN increase significantly with increasing discharge power, especially for longer treatment times of 30 and 40 min, while the increase is more moderate for treatment times of 10 and 20 min, and the concentrations remain almost constant at discharge powers exceeding 150 W. It should be noted that, although the concentrations of NO_3^- and TN increase linearly with time in an ideal scenario, in reality, the increasing rate of NF products slows with increasing treatment time, which may be due to hindered in-liquid diffusion and lower pH. However, in our work, the flowing water can carry away the accumulated products in the liquid phase; thus, this effect can be weakened, which is beneficial for the production of NO_3^- and TN in PAW. As demonstrated in Fig. 8(c), the liquid interface temperature decreases from 95 °C in static water to 50 °C in the flowing water, and the bulk liquid phase temperature declines from 61 °C to 33 °C at a high power (200 W), which indicates that the flowing water can enhance the heat-transfer process. Moreover, this temperature reduction can enhance the solubility of gaseous components NO_x, thereby promoting the production of dissolved species such as NO_3^- and TN. On the other hand, as the pH decreases over time, the solubility of NO decreases, which may lead to the curve plateaus in Fig. 8. Finally, maximum concentrations of 154 mg L^{-1} and 199 mg L^{-1} for NO_3^- and TN, respectively, are obtained at a discharge power of 200 W and treatment time of 40 min. For comparison, Bolouki *et al.*[44] obtained a maximum concentration of only 40 mg L^{-1} NO_x by changing the input gas type and processing time using DBD plasma over a water surface.

It is worth noting that the concentration difference between NO_3^- and TN is very small—the maximum difference is only 18% of the TN concentration—indicating that the main nitro-

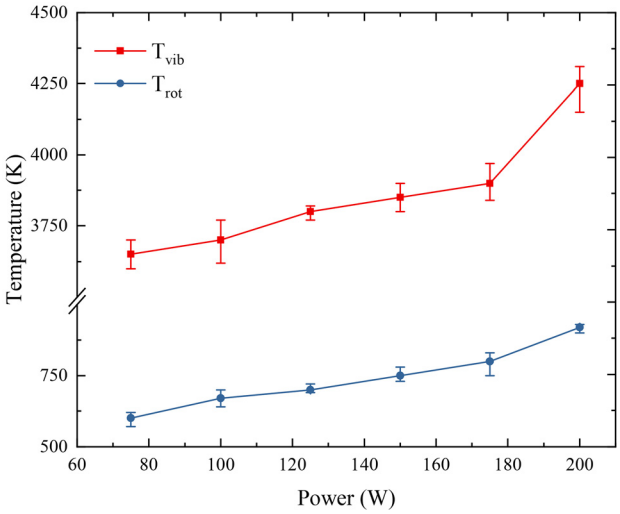

Fig. 6 Dependence of T_{vib} and T_{rot} on the input power at an air flow rate of 0.5 L min^{-1}.

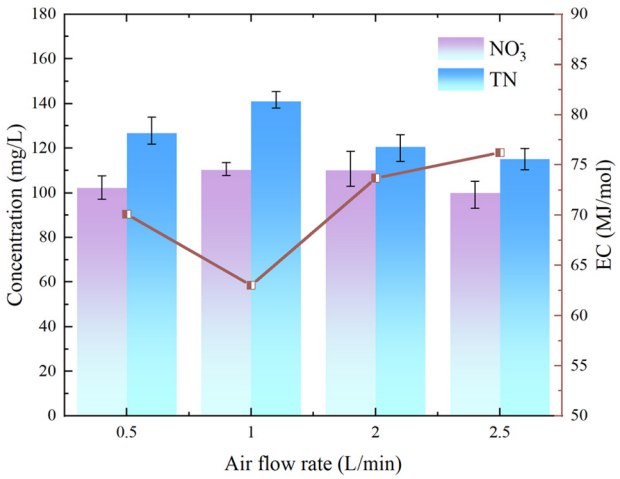

Fig. 7 Variations in NO_3^- and TN concentrations and energy consumption with air flow rate at a treatment time of 30 min and an input power of 150 W.

gen-containing compound in the PAW is NO_3^-, and the concentration of NO_2^- is very low. This is because the plasma phase contains a large number of highly oxidizing species (*e.g.* O atoms, O_3), which lead to either rapid oxidation of NO to NO_2 in the gas phase or oxidation of NO_2^- to NO_3^- in the liquid phase. Note that the temperature is lower in DBD compared to a spark discharge and gliding arc plasma, so NO is more likely to form NO_2 in the gas phase,[45] since the reaction rate coefficients of NO + O → NO_2 and NO + O → N + O_2 are 4.2×10^{-18} cm^3 s^{-1} and 1.28×10^{-23} cm^3 s^{-1}, respectively, at a gas temperature of 600 K, and the former is an exothermic reaction, while the latter is an endothermic reaction. Subsequently, NO and NO_2 can dissolve in the water, giving rise to NO_2^- and NO_3^-. NO_2^- can be further oxidized by oxidizing species (*e.g.* H_2O_2, O_3 and OH radicals) to yield NO_3^- in the water. Lukes *et al.* also pointed out that the NO_2^- concentration produced in liquid is negligible for a DBD discharge, while it is even larger than the NO_3^- concentrations in a spark discharge.[46]

3.1.4. Analysis of the underlying mechanisms of NF. The chemical kinetics and mechanisms of NF in both the gas and liquid phases are presented schematically in Fig. 9. The excited species N_2(C) and N_2(A), as well as O, O(^{1}D) and OH radicals detected by OES, are typically produced by the electron impact reactions (R1)–(R5) shown in Table 2, and may be precursor species for the NF.

NO is typically formed *via* the Zeldovich mechanism, which includes the reaction between O atoms and N_2 molecules, as well as the reaction between N atoms and O_2 molecules ((R6) and (R7) in Table 2). Furthermore, the Einstein coefficients of OH and O atomic emission lines are 6.22×10^5 s^{-1} and 3.69×10^7 s^{-1}, respectively. As the emission intensity of OH radicals is about 20 times larger than that of O atoms (see Fig. 5), this may indicate that the reaction between OH radicals and N atoms ((R8) in Table 2) could also be a pathway for NO production.[53]

Once NO is formed, it can be further oxidized by O atoms or O_3 to produce NO_2 *via* reactions (R9) and (R10).[46] However, reactions of NO_2 with O atoms may also contribute to the formation of NO by (R11), resulting in an equilibrium of NO and NO_2 in the gas (plasma) phase. In addition to reaction (R5), OH radicals in the plasma phase can also be produced by reaction (R12) and participate in the generation of H_2O_2, HNO_2, and HNO_3 in the gas phase *via* reactions (R13)–(R15), which are the main production reactions of these species in the gas phase.[34] Thus, it is inferred that HNO_2 and HNO_3 can be transported from the plasma phase to the liquid phase through the plasma–liquid interface and play a role in the production of nitrate and nitrite. HNO_2 and HNO_3 can be dissolved in water to produce NO_2^-, NO_3^- and H^+, making the solution acidic.[54]

As discussed in ref. 51, the accumulation of NO_2^- and NO_3^- in the liquid phase may not only be due to the dissolution of neutral compounds from the plasma phase, but may also be due to reactions of NO and NO_2 with short-lived OH radicals (reactions (R17) and (R18)) and with H_2O (reactions (R19) and (R20)) in the liquid phase.

As illustrated in Fig. 8, the concentration difference between NO_3^- and TN in the liquid phase is very small, indicating less accumulation of NO_2^- in the liquid phase. This is because of oxidation processes of NO_2^- to NO_3^- in the water, such as (R21) in Table 2.

Now that we know the performance of the NF and the basic mechanisms, we investigated whether the combination of plasma with TiO_2 and/or UV can further improve the performance.

3.2 NF with the air DBD plasma + TiO_2 + UV coupled system

3.2.1 Variations of NO_3^- and TN concentrations. Fig. 10 illustrates the concentrations of NO_3^- and TN in pure plasma, plasma + TiO_2, plasma + UV, and plasma + TiO_2 + UV coupled conditions, for a treatment time of 20 min. At input powers lower than 125 W, the NO_3^- concentrations in plasma + TiO_2

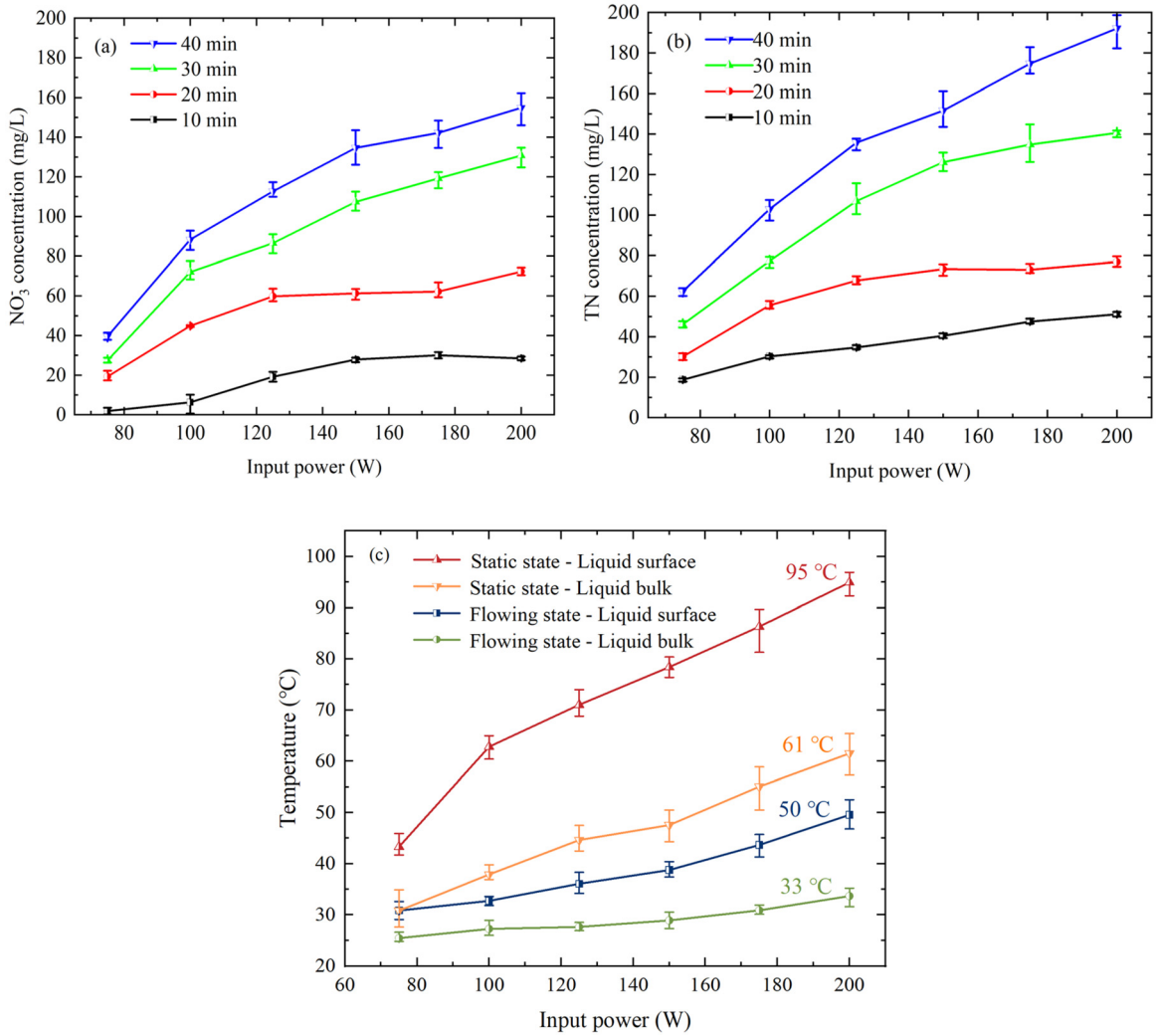

Fig. 8 Variations in NO_3^- (a) and TN (b) concentrations with the input power for different treatment times, and variations in the measured temperature in the static and flowing waters by supplying the input power for 10 min (c).

and plasma + UV conditions are basically the same as those obtained with plasma alone, while the concentration of TN increases significantly under plasma + UV conditions, which indicates that the concentration of NO_2^- in the liquid phase increases significantly. At higher powers, the NO_3^- and TN concentrations under plasma + TiO_2 and plasma + UV conditions are slightly higher, indicating that UV and TiO_2 play a role at powers above 125 W. Experiments under "UV only" and "TiO_2 only" conditions are also performed, which indicated that only UV irradiation or only TiO_2 catalysis almost had no contribution to the production of NO_3^- and TN.

When coupling plasma with TiO_2 and UV, the NO_3^- and TN concentrations rise more significantly, except at the lowest power of 75 W, with the maximum enhancements of 57% and 45%, respectively, at input powers of 200 W. In this case, the concentration difference between NO_3^- and TN is relatively small, indicating that the main nitrogen-containing product is NO_3^-. As shown in Fig. 10(c), the pH value is lowest in the coupled plasma + TiO_2 + UV system, which is consistent with the variation of the NO_3^- and TN concentrations. According to the charge conservation of ions in the solution, the calculated pH values are 2.9 and 2.7 at a power of 200 W for pure plasma and plasma + TiO_2 + UV systems, respectively, while the measured pH values are about 3.0 and 2.5, respectively. The calculated and experimental pH values are generally in good agreement, thus confirming that NH_4^+ is present in negligible quantities and most NF goes through NO_x. We also conducted stability test experiments for the plasma + TiO_2 + UV system, which are rigorously repeated ten times in succession, with experimental time of 20 min each and input power of 200 W. As illustrated in Fig. 10(d), the NO_3^- concentration remained at about 110 mg L^{-1} with a small fluctuation range ±7 mg L^{-1}, and the TN concentration was maintained at approximately 115 mg L^{-1} across all the experiments, demonstrating a negligible catalyst activity loss within this system and highlighting the practical application potential of the plasma + TiO_2 + UV system.

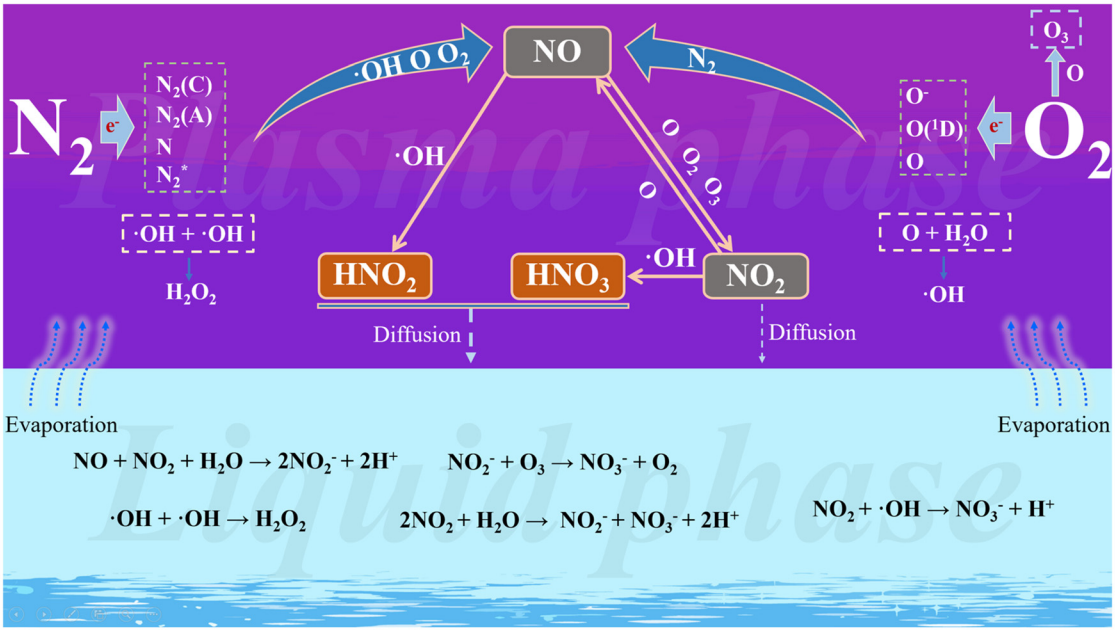

Fig. 9 Mechanisms of nitrogen fixation in the plasma and water regions.

Table 2 Possible chemical reaction pathways for NF in our experiment

No.	Chemical reactions	Rate coefficient k ($cm^3\ s^{-1}$ for two-body, and $cm^6\ s^{-1}$ for three-body reactions) cross section σ (E) [cm^2]	Ref.
R1	$e + N_2(X) \rightarrow N_2(A) + e$	σ (E)	47
R2	$e + N_2(X) \rightarrow N_2(B) + e$	σ (E)	41
R3	$e + N_2(X) \rightarrow N_2(C) + e$	σ (E)	47
R4	$e + O_2 \rightarrow O + O(^1D) + e$	σ (E)	41
R5	$e + H_2O \rightarrow OH + H + e$	σ (E)	41
R6	$O + N_2(A) \rightarrow NO + N$	7×10^{-12}	47
R7	$N + O_2 \rightarrow NO + O$	$1.1 \times 10^{-14} T_g$ (K) exp[−3150/T_g (K)]	47
R8	$N + OH \rightarrow NO + H$	4.7×10^{-11}	48
R9	$NO + O + M \rightarrow NO_2 + M$	1×10^{-31} [298/T_g (K)]$^{1.5}$	47
R10	$NO + O_3 \rightarrow NO_2 + O_2$	4.3×10^{-12} exp[−1560/T_g (K)]	41
R11	$NO_2 + O \rightarrow NO + O_2$	8×10^{-12} [T_g (K)/300]$^{0.18}$	41
R12	$O(^1D) + H_2O \rightarrow 2{\cdot}OH$	1.6×10^{-10} exp[64/T_g (K)]	41
R13	$OH + OH \rightarrow H_2O_2$	1.5×10^{-11} [T_g (K)/300]$^{-0.37}$	41
R14	$NO + OH \rightarrow HNO_2$	3.3×10^{-11}	49
R15	$NO_2 + OH \rightarrow HNO_3$	4×10^{-12}	49
R16	$NO_2 + NO_3 \rightarrow N_2O_5$	1.9×10^{-12} [T_g (K)/300]$^{0.2}$	50
R17	$NO_{2(aq)} + OH_{(aq)} \rightarrow NO_3^-{}_{(aq)} + H^+{}_{(aq)}$	3.3×10^{-11}	51
R18	$NO_{(aq)} + OH_{(aq)} \rightarrow NO_2^-{}_{(aq)} + H^+{}_{(aq)}$	2×10^{-11}	51
R19	$2NO_{2(aq)} + H_2O_{(aq)} \rightarrow NO_2^-{}_{(aq)} + NO_3^-{}_{(aq)} + 2H^+{}_{(aq)}$	1.32×10^{-34}	52
R20	$NO_{(aq)} + NO_{2(aq)} + H_2O_{(aq)} \rightarrow 2NO_2^-{}_{(aq)} + 2H^+{}_{(aq)}$	5.55×10^{-34}	52
R21	$NO_2^-{}_{(aq)} + O_{3(aq)} \rightarrow NO_3^-{}_{(aq)} + O_{2(aq)}$	6.15×10^{-16}	51

3.2.2 Insights into the chemistry. In this section we analyze the underlying mechanisms under different conditions to explain the variations of NO_3^- and TN concentrations. Fig. 11 presents the measured emission spectrum for the pure plasma and plasma + UV + TiO_2 experiments. The emission intensities of different spectral lines and bands are basically the same in these two cases, except at the wavelength of 386 nm, which is caused by the external UV light source with a central wavelength of 385 nm and a bandwidth of 40 nm. Therefore, we may conclude that the addition of UV and TiO_2 mainly affects the chemical reactions in the liquid phase, and has little effect on the processes in the plasma (gas phase).

When UV light with an intensity of about 0.02 W cm^{-3} is introduced, H_2O_2 produced by OH recombination at the plasma–liquid interface (R13) will undergo photolysis through (R22),[44] and O_3 and H_2O will decompose by (R23). Although H_2O_2 and O_3 can yield OH radicals by (R24) in the absence of UV light, more OH radicals can be produced by (R22) and (R23) at the interface when UV light is present,[55] promoting

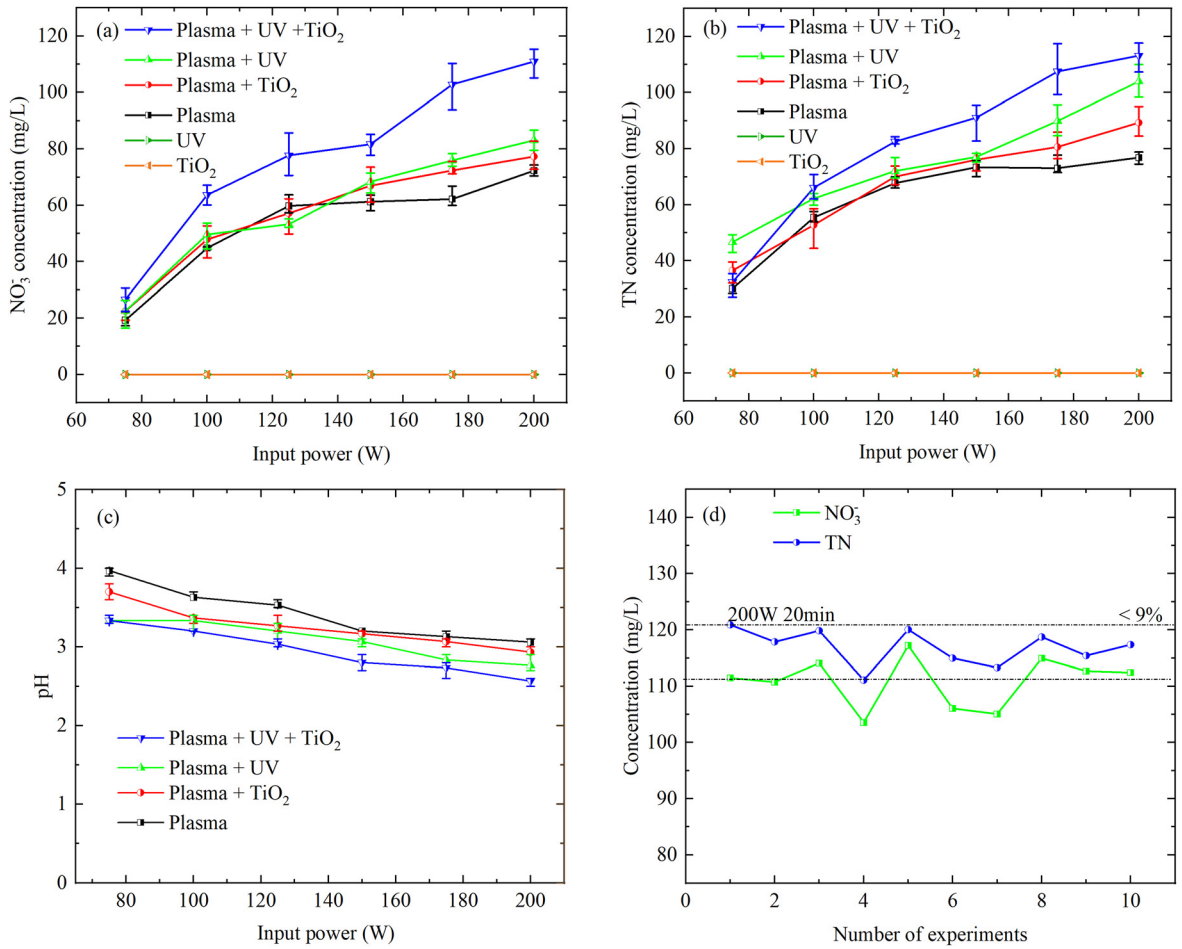

Fig. 10 Variations in NO_3^- (a) and TN (b) concentrations and pH (c) with the input power for a treatment time of 20 min for plasma, only UV, only TiO_2, plasma + UV, plasma + TiO_2 and plasma + UV + TiO_2 conditions, and variations in NO_3^- and TN concentrations with repeated experiments (d).

the reactions (R17) and (R18) in Table 2, which can explain the rise in concentration of NF products. With increasing power, more H_2O_2 and O_3 will be formed, and thus participate in (R22) and (R23), which is consistent with the obvious increase in concentrations of NF products at high power shown in Fig. 10.

$$H_2O_2 + h\nu \rightarrow 2^{\bullet}OH \quad \text{(R22)}$$

$$H_2O + O_3 + h\nu \rightarrow 2^{\bullet}OH + O_2 \quad \text{(R23)}$$

$$H_2O_2 + 2O_3 \rightarrow 2^{\bullet}OH + 3O_2 \quad \text{(R24)}$$

TiO_2 has a band gap of 3.2 eV for the rutile mineral phase and is a widely used photocatalyst. It can be activated by forming electron–hole pairs with sufficient photon energy. The defect disorders (V_o) in the photocatalyst play an important role in catalysis, and are considered to be the active site of adsorption and activation of reactants in photocatalytic reactions.[56] Fig. 12 shows the Ti 2p XPS deconvolution spectra of TiO_2. Two peaks are identified, corresponding to $Ti_{3/2}$ and $Ti_{1/2}$, respectively, which can be deconvolved into four peaks. The two binding energy peaks of Ti^{4+} are 459.0 eV and 464.6 eV, respectively, and the two binding energy peaks of Ti^{3+} are located near 458.6 eV and 463.9 eV, respectively. The presence of Ti^{3+} indicates that part of the Ti^{4+} (of TiO_2) has changed, which is often accompanied by the formation of V_o due to local charge balance.

$$TiO_2 + h\nu \rightarrow TiO_2\ (e^- + h^+) \quad \text{(R25)}$$

$$2Ti^{4+} + O^{2-} \rightarrow V_o + 2Ti^{3+} + \frac{1}{2}O_2 \quad \text{(R26)}$$

In fresh TiO_2, only Ti^{4+} exists, while Ti^{3+} is found in the plasma + TiO_2 system. When UV is introduced into the system, it can be observed that Ti^{3+} increases significantly, indicating the formation of more oxygen vacancies (V_o) that serve as active sites for charge separation. This phenomenon aligns with the studies by Khan *et al.*,[57] where Ti^{3+}-V_o complexes enhanced photogenerated carrier separation by acting as electron traps, transferring electrons from the conduction band of TiO_2 and holes from the valence band through (R27)–(R30), followed by the generation of highly oxidizing species, *i.e.*,

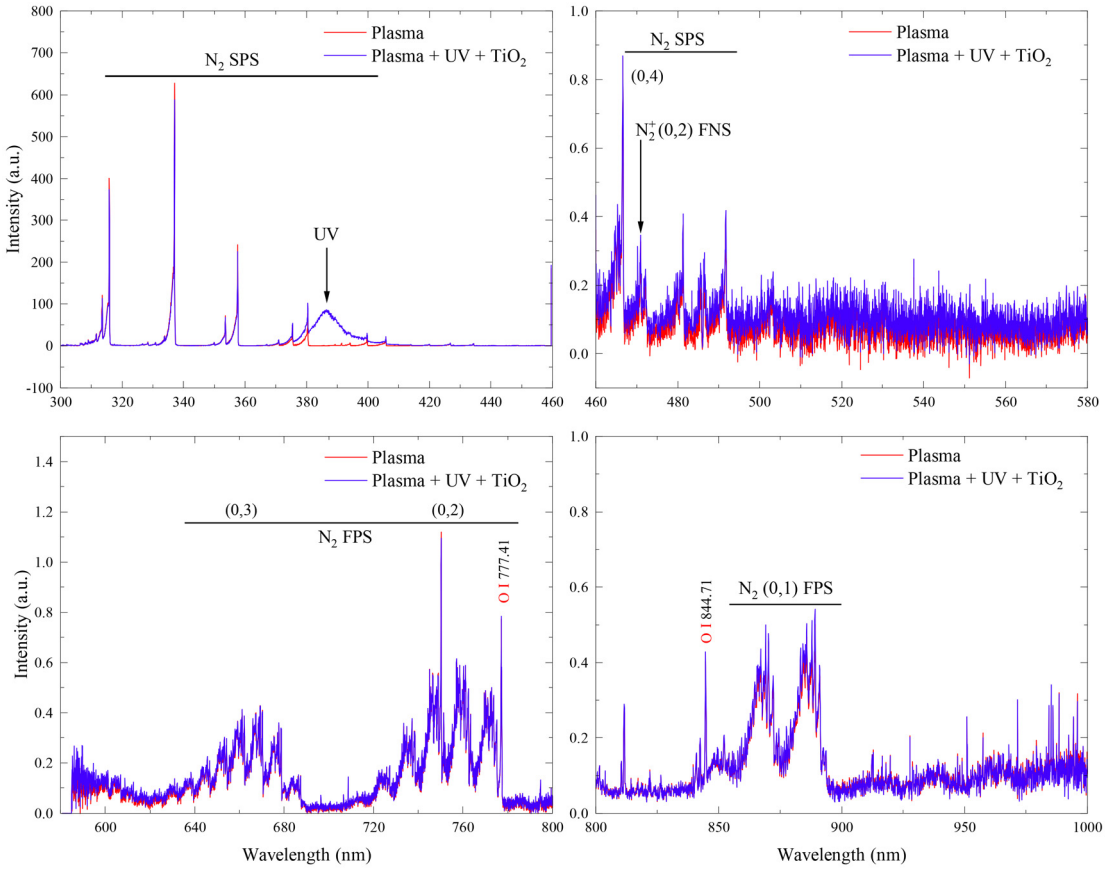

Fig. 11 Measured emission spectra in the pure plasma and plasma + UV + TiO_2 experiments.

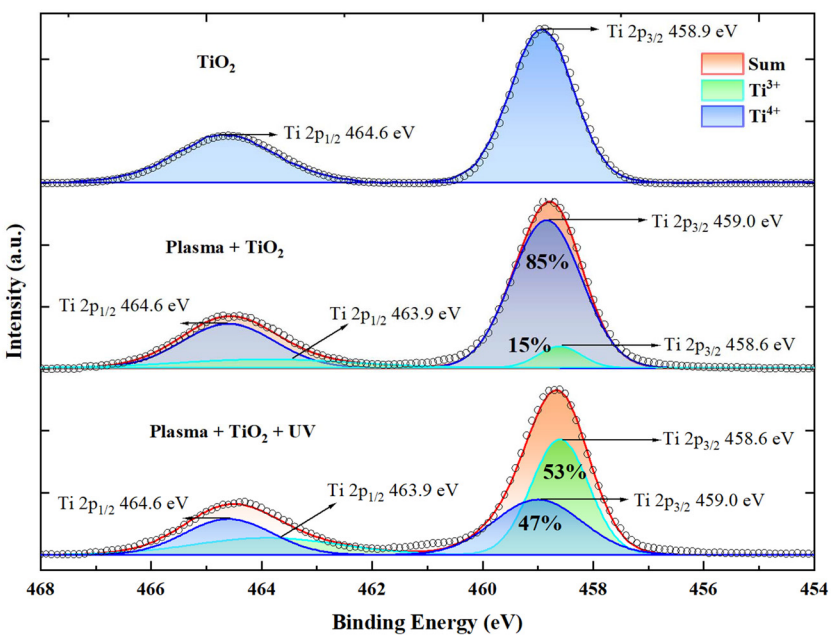

Fig. 12 XPS spectra of Ti 2p peaks for TiO_2.

OH.[58] OH plays a crucial role in the subsequent oxidation of N to NO_3^- and NO_2^-, see (R8) in Table 2.

$$H_2O + h^+ \rightarrow {}^{\bullet}OH + H^+ \quad (R27)$$

$$H_2O + e^- \rightarrow {}^{\bullet}OH + H^+ + 2e^- \quad (R28)$$

$$O_2 + e^- \rightarrow 2{}^{\bullet}O + e^- \quad (R29)$$

$$H_2O + O \rightarrow 2{}^{\bullet}OH \quad (R30)$$

Fig. 13 summarizes the mechanisms of NF in the liquid phase under the synergistic effect of plasma, TiO_2 and UV light. For the plasma + TiO_2 system, at low power, the intensity of UV light generated by the plasma discharge is weak, so the photocatalytic effect is obviously weak. However, as the input power increases, the UV light emitted by the plasma discharge also increases. We integrated the light intensity in the wavelength range from 200 nm to 385 nm, in which the TiO_2 photocatalytic effect is induced. When the input power increases from 75 W to 200 W, the light intensity produced by DBD itself increases from 95 μW cm^{-3} to 188 μW cm^{-3}. TiO_2 absorbs more photons, which, in turn, produce more electrons and holes, resulting in a greater increase in the NO_3^- and TN concentrations at higher power, as shown in Fig. 10. This indicates that the catalytic effect of TiO_2 will be enhanced with increasing input power, due to the UV light produced by the plasma, resulting in an increase in NF products. However, compared with the UV light intensity, the UV radiation ($\lambda \leq 385$ nm) produced by the air plasma discharge is still very weak, so the NO_3^- and TN concentrations are significantly increased in the plasma + UV + TiO_2 system.

As presented in Fig. 12, the Ti^{3+} percentage in the plasma + TiO_2 + UV system is 53%, compared to 15% in the plasma + TiO_2 system (without UV). This indicates that the plasma + TiO_2 + UV system forms more active sites (V_o) and thus improves the catalytic efficiency of TiO_2, which promotes the production of more OH in the liquid phase. Thus, the transport of NO and NO_2 from the gas to the liquid phase is enhanced, and the oxidation process of NO_2^- to NO_3^- is more prominent, which can explain why the rise in NO_3^- concentration is much higher than that of TN in the case of the plasma + UV + TiO_2 coupled system. For example, at a power of 100 W, compared with the plasma-only system, the NO_3^- concentration increases from 45 mg L^{-1} to 64 mg L^{-1}, while the TN concentration rises from 55 mg L^{-1} to 66 mg L^{-1}. Hence, the enhancement of NO_3^- and TN concentrations is 42% and 15%, respectively, leading to a relatively small difference between NO_3^- and TN concentrations in the plasma + TiO_2 + UV system.

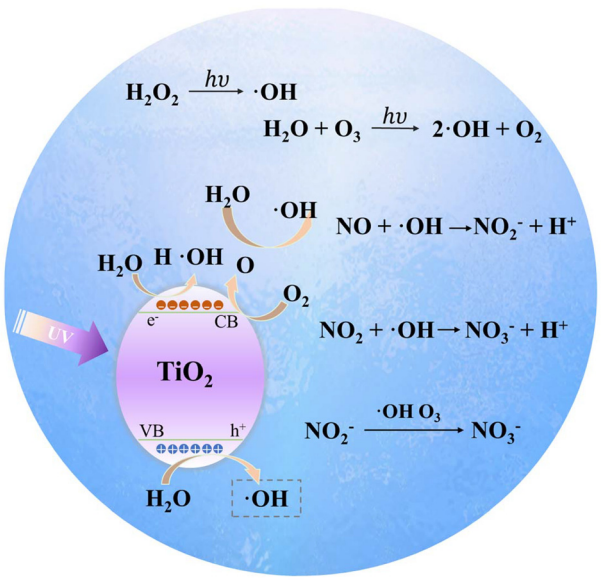

Fig. 13 Mechanism of NF in the liquid phase under the synergistic effect of plasma, TiO_2 and UV light.

3.3 Energy consumption of NF and NO_x production rate in the various systems

The variation of EC and production rate of NO_x as a function of input power for different treatment times, in the case of the plasma-only system, is presented in Fig. 14(a) and (b). The EC first shows a decreasing trend, and then increases with rising power. The minimum value of 61 MJ mol^{-1} is reached at a treatment time of 10 min, and at a lower input power of 100 W. The higher EC at an input power of 75 W is probably because the weak discharge, with only a limited number of micro-discharge filaments shown in Fig. 4, leads to a low concentration of NF products. At constant treatment time, upon increasing the input power, the TN concentration rises less than linearly with power (Fig. 8(b)), which explains the rise in the EC. In contrast to the variation trend of EC, the production rate of NO_x increases with increasing input power, and has a higher value at a treatment time of 10 min. The maximum value of 162 μmol min^{-1} is reached at a processing time of 10 min and an input power of 200 W. In summary, the use of relatively short treatment times and an intermediate input power results in the lowest EC for NF; however, to achieve higher TN concentrations and production rates, larger input powers are required.

In Fig. 15, the EC and production rate of NO_x are compared under different plasma conditions. Compared with the pure plasma system, Fig. 15 shows that the minimum EC values for the plasma + UV and plasma + TiO_2 cases are not much lower than that of the pure plasma, although their TN concentrations increase. The enhancement effect for the plasma + UV and plasma + TiO_2 cases is strengthened with increasing input power, especially at a power of 200 W, where the EC measured under the plasma + UV and plasma + TiO_2 conditions drops by 21 and 13%, respectively, compared to the pure plasma condition, which is in line with the results shown in Fig. 10. Finally, the lowest obtained EC is 60 MJ mol^{-1} for the plasma + UV + TiO_2 case, and it drops by 11% compared with the pure plasma condition, as shown in Fig. 15(a). Furthermore, the EC in the plasma + UV + TiO_2 system was 28% lower than that of the plasma system at the highest input power of 200 W.

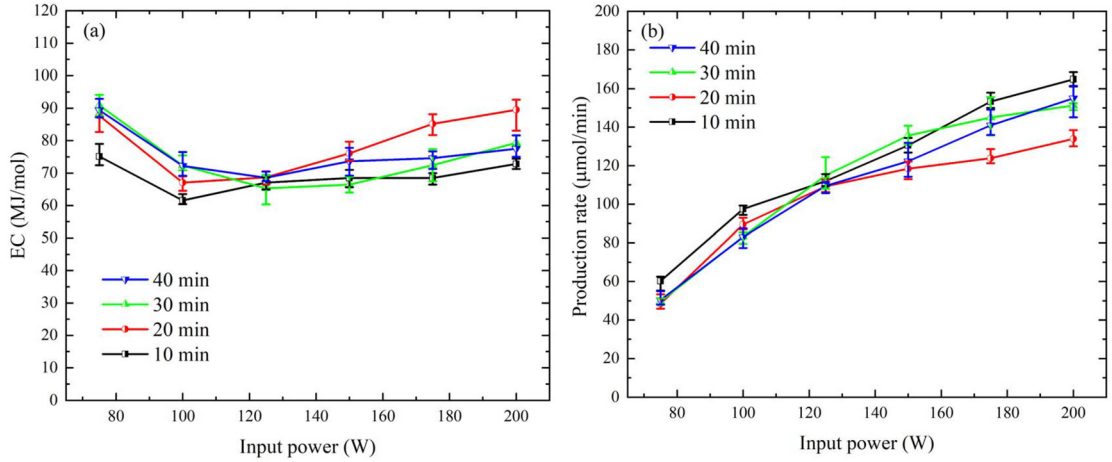

Fig. 14 Variations in EC (a) and production rate of NO_x (b) with input power for different treatment times at a gas flow rate of 0.5 L min^{-1} for the plasma-only case.

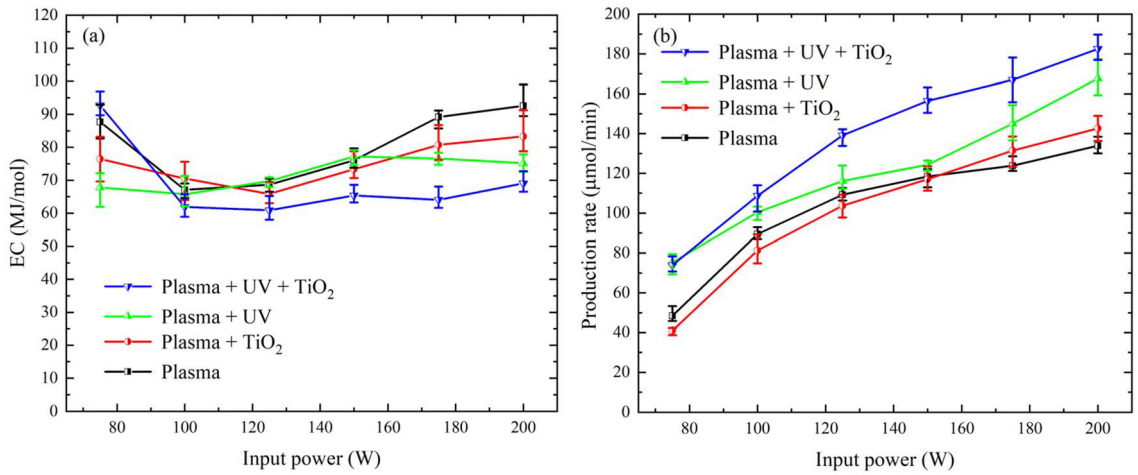

Fig. 15 Variations in EC (a) and production rate of NO_x (b) with input power at a treatment time of 20 min and gas flow rate of 0.5 L min^{-1} for plasma only, plasma + UV, plasma + TiO_2 and plasma + UV + TiO_2 cases.

As presented in Fig. 15(b), the production rate is also highest under the plasma + UV + TiO_2 system, which is consistent with the variation of concentrations shown in Fig. 10. The production rate of NO_x increases from 133 μmol min^{-1} under pure plasma conditions to 182 μmol min^{-1} in the plasma + UV + TiO_2 system at a power of 200 W. Production rates of TN using DBD plasma are reported to be relatively low.[44,53] Bolouki *et al.* achieved a TN production rate of only 6 μmol min^{-1} by using DBD plasma.[44] Roy *et al.* obtained a high TN concentration of 600 mg L^{-1} with only 5 mL of water by using DBD plasma over water, but the corresponding production rate of TN was only 4.8 μmol min^{-1}.[53] So, the improvement presented here with the plasma + UV + TiO_2 case is obvious for both the EC and production rate compared with the only plasma condition, not only in the current experiments but also in comparison with the literature.

3.4. Comparisons with other pure plasma and plasma–liquid NF technologies

A comparison of the results of our work with those of recent studies on only plasma[10,20,21,59–64] and plasma–liquid[19,28,29,31,53,65–69] NF is presented in Fig. 16, in terms of reported NO_x concentrations and EC. The EC of nitric acid produced *via* the combined Haber–Bosch (H–B) and Ostwald process is also given in Fig. 16.

Due to the possible incomplete absorption of the gaseous NO_x products by the liquid (see plateauing in Fig. 8) and the fact that the system we used was not specifically optimised, we can see that the EC of our plasma–liquid system is higher than that of plasma only gas phase systems. Moreover, the presence of water can be detrimental due to the energy losses caused by energy spent on water evaporation.[52,70] However, the gas-phase

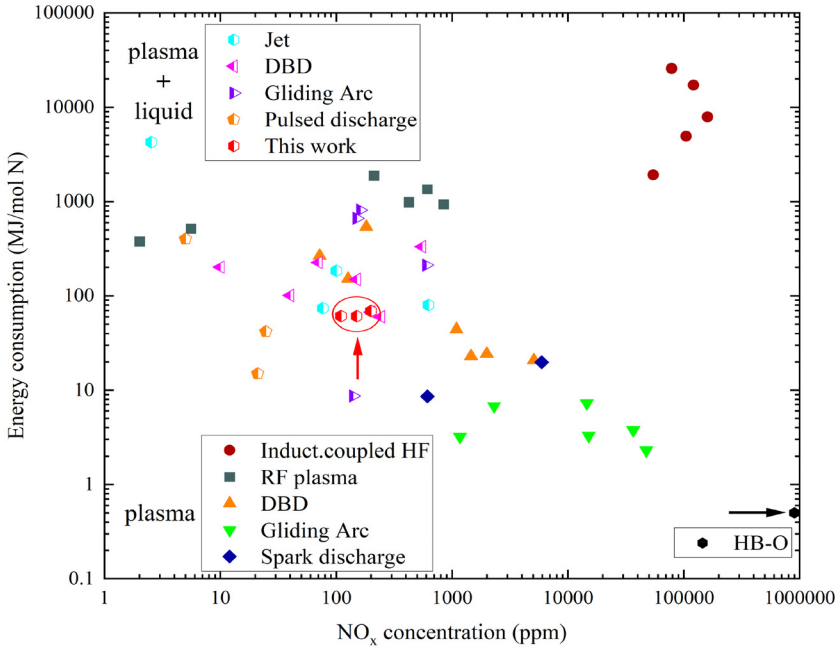

Fig. 16 Comparison of energy consumption for NO_x production in various plasma reactors. The pure gas-phase plasma systems are indicated with full symbols, while the plasma–liquid systems are indicated with half-open symbols. The Haber–Bosch + Ostwald (HB–O) benchmark is also indicated.

NF process primarily produces NO_x, while HNO_3, a more versatile and directly applicable nitrogen product, can only be produced in the presence of water. This aqueous-phase conversion significantly broadens the application potential of plasma-based NF, particularly for decentralized, on-site fertilizer production, where HNO_3 can be readily absorbed or reacted to form stable compounds.[17] Here, in our study, NO oxidation and further dissolution into HNO_x are achieved by a one-pot method, while making NO_x first and then dissolving them in liquid require large washing systems due to the generally suboptimal solubility of NO in water. Thus, we emphasize the importance of studying plasma–water systems.

In our work, by introducing TiO_2 + UV for collaborative catalysis and using flowing water to reduce the working temperature and transfer the NF products, an EC of about 60 MJ mol^{-1} was obtained by the device using DBD with flowing water as the ground electrode, which is similar to the EC of 56–140 MJ mol^{-1} in gas-phase DBD.[59] Furthermore, DBD systems typically exhibit higher ECs than warm plasmas; therefore, if a warm plasma–liquid system (*e.g.*, GA) is developed, the EC may be reduced, but the NO_x concentration may also decrease. Compared with other plasma–liquid NF results in the literature, we obtained a relatively high NO_x concentration and low EC, except for the work by Dinh *et al.*, which reported an EC of about 8 MJ mol^{-1},[29] but this was upon the introduction of an ozone generator, which obviously increases the operational complexity of the system. Gorbanev *et al.*[2] also achieved a low EC of 15 MJ mol^{-1} using pulsed discharge; however, the NO_x concentrations were much lower than our results. Lamichhane *et al.* employed AC discharge and incorporated TiO_2 + UV in their experiments. The results indicated that, compared to the 13 mg L^{-1} concentration and 1000 MJ mol^{-1} energy consumption in the case of pure plasma, within the plasma + TiO_2 + UV system, the NO_x concentration was elevated to 26 mg L^{-1} while the energy consumption was reduced to 300 MJ mol^{-1}.[33] Contrasted with pure plasma system, Sun *et al.*[32] demonstrated that plasma combined with photocatalysis can reduce the EC from 140 MJ mol^{-1} to 50 MJ mol^{-1}. Nevertheless, the treatment water volume of the aforementioned photocatalytic system was relatively limited, thereby resulting in product generation rates of only 1.3 and 3.5 μmol min^{-1}. This hinders its large-scale industrial promotion and application. Finally, it is worth mentioning that, compared with other plasma sources, our DBD device is simple and has a larger discharge area, which can achieve large-area plasma–liquid interaction treatment, while the flowing water reduces the temperature and enables the device to work for prolonged periods at increased power, which is of great value for PAW industrial applications.

In the H–B process, ammonia is synthesized from hydrogen and atmospheric nitrogen, then the produced NH_3 is oxidized in the Ostwald process to form NO and NO_2, which are subsequently absorbed in water to form HNO_3. The substantially lower energy cost for NF *via* the H–B and Ostwald process is about 0.5–0.6 MJ mol^{-1} N.[10] However, considering environmental impacts, the H–B process requires the use of catalysts and must be conducted at high temperature and pressure. Maintaining these reaction conditions consumes large amounts of chemical fuels and emits greenhouse gases such as carbon dioxide, with 1.94 kg of CO_2 emitted per 1 kg of

nitrogen fixed.[71] In contrast, the current method does not strictly require catalysts and, if combined with renewable energy sources such as solar or wind power, the entire production process can achieve zero carbon emissions. These advantages highlight the significant potential of this method in advancing carbon-neutral nitrogen fixation.

4. Conclusions

In this study, we designed a novel DBD reactor with continuous flowing water to synthesize a nitrogen fertilizer solution from air. The plasma can be easily coupled with UV and TiO_2 in the water to further improve the NF efficiency. The maximum NO_3^- concentration and minimum EC under pure plasma conditions are 154 mg L^{-1} and 61 MJ mol^{-1}, respectively. At 200 W and 20 min treatment time, compared to the case of pure plasma, adding TiO_2 and irradiation with UV results in a significant increase in the NO_3^- and TN concentrations (by *ca.* 50% each) and a drop in the EC (by 28%).

X-ray photoelectron spectroscopy analysis reveals the mechanism of TiO_2 and UV enhancement for NF. It is found that, compared with the original TiO_2 particles, the presence of Ti^{3+} increases to 15% and 53% in the plasma + TiO_2 system and the plasma + TiO_2 + UV system, respectively, indicating the formation of more electron–hole pairs. Thus, the catalytic efficiency of TiO_2 is improved, which can promote the production of more OH radicals in the liquid phase, and thus enhance the NF process. In general, our work demonstrates the possibility of improving the NO_x production and reducing the EC in a combined plasma + UV + TiO_2 coupled system. Future work will focus on the large-scale implementation of this coupled system to realize highly efficient nitrogen fertilizer production.

Conflicts of interest

There are no conflicts to declare.

Data availability

The data supporting this article have been included as part of the SI. Measurement method of NO_3^- and TN concentrations; calculation of mean electric field, reduced electric field strength and electron temperature; supplemental results of OES, rotational and vibrational temperature measurement. See DOI: https://doi.org/10.1039/d5gc02201k.

Acknowledgements

This work was supported by the National Natural Science Foundation of China (Grant No. 12375245, 12535016, 12005010 and 12175011), and the Fundamental Research Funds for the Central Universities (YWF-23-L-1221).

References

1 C. Smith, A. K. Hill and L. Torrente-Murciano, *Energy Environ.*, 2020, **13**, 331–344.
2 Y. Gorbanev, E. Vervloessem, A. Nikiforov and A. Bogaerts, *ACS Sustainable Chem. Eng.*, 2020, **8**, 2996–3004.
3 P. Mehta, P. M. Barboun, Y. Engelmann, Y. Eng, D. B. Go, A. Bogaerts, W. F. Schneider and J. C. Hicks, *ACS Catal.*, 2020, **10**, 6726–6734.
4 L. F. Razon, *Environ. Prog. Sustainable Energy*, 2014, **33**, 618–624.
5 B. S. Patil, Q. Wang, V. Hessel and J. Lang, *Catal. Today*, 2015, **256**, 49–66.
6 M. Van Der Hoeven, Y. Kobayashi and R. Diercks, *Technology roadmap: Energy and GHG reductions in the chemical industry via catalytic processes*, International Energy Agency, Paris, 2013, p. 56.
7 V. D. Rusanov, A. A. Fridman and G. V. Sholin, *Soviet Phys. – Usp.*, 1981, **24**, 447.
8 K. R. Birkeland, *Trans. Faraday Soc.*, 1906, **2**, 98–116.
9 B. S. Patil, V. Hessel, L. C. Seefeldt, D. R. Dean and B. M. Hoffman, *Ullmann's Encyclopedia of Industrial Chemistry*, 2017.
10 K. H. R. Rouwenhorst, F. Jardali, A. Bogaerts and L. Lefferts, *Energy Environ. Sci.*, 2021, **14**, 2520–2534.
11 V. V. Kovačević, B. P. Dojčinović, M. Jović, G. M. Roglić, B. M. Obradović and M. M. Kuraica, *J. Phys. D: Appl. Phys.*, 2017, **50**, 155205.
12 Z. Liu, Y. Tian, G. Niu, X. Wang and Y. Duan, *ChemSusChem*, 2021, **14**, 1507–1511.
13 T. Sakakura, Y. Takatsuji, M. Morimoto and T. Haruyama, *Electrochemistry*, 2020, **88**, 190–194.
14 N. C. Roy, N. Maira, C. Pattyn, A. Reny, M. P. Delplance and F. Reniers, *Chem. Eng. J.*, 2023, **461**, 141844.
15 I. M. Piskarev and I. P. Ivanova, *Plasma Sources Sci. Technol.*, 2019, **28**, 085008.
16 E. Vervloessem, Y. Gorbanev, A. Nikiforov, N. D. Geyter and A. Bogaerts, *Green Chem.*, 2022, **24**, 916–929.
17 E. Vervloessem, M. Gromov, N. D. Geyter, A. Bogaerts, Y. Gorbanev and A. Nikiforov, *ACS Sustainable Chem. Eng.*, 2023, **11**, 4289–4298.
18 J. Yang, T. Li, C. Zhong, X. Guan and C. Hu, *J. Electrochem. Soc.*, 2016, **163**, E288.
19 J. Pawłat, P. Terebun, M. Kwiatkowski, B. Tarabová, Z. Kovaľová, K. Kučerová, Z. Machala, M. Janda and K. Hensel, *Plasma Chem. Plasma Process.*, 2019, **39**, 627–642.
20 E. Vervloessem, M. Aghaei, F. Jardali, N. Hafezkhiabani and A. Bogaerts, *ACS Sustainable Chem. Eng.*, 2020, **26**, 9711–9720.
21 F. Jardali, S. Van Alphen, J. Creel, H. A. Eshtehardi, M. Axelsson, R. Lngels and A. Bogaerts, *Green Chem.*, 2021, **23**, 1748–1757.
22 S. V. Alphen, H. A. Eshtehardi, C. O'Modhrain, J. Bogaerts, H. V. Poyer, J. Greel, M. P. Delpancke, R. Snyders and A. Bogaerts, *Chem. Eng. J.*, 2022, **443**, 136529.
23 I. Tsonev, C. O'Modhrain, A. Bogaerts and Y. Gorbanev, *ACS Sustainable Chem. Eng.*, 2023, **11**, 1888–1897.

24 S. Kelly and A. Bogaerts, *Joule*, 2021, **5**, 3006–3030.
25 I. Tsonev, H. A. Eshtehardi, M. P. Delplancke and A. Bogaerts, *Sustainable Energy Fuels*, 2024, **8**, 2191–2209.
26 L. Xiong, L. Feng, M. Nie, D. Li, Z. Zhang, C. Liu, Z. Dai, Y. Xiao and Y. Xu, *Foods*, 2024, **13**, 703.
27 Y. Gao, K. Francis and X. Zhang, *Food Res. Int.*, 2022, **157**, 111246.
28 T. Haruyama, T. Namise, N. Shimoshimizu, S. Uemura, Y. Takatsuji, M. Hino, R. Yamasaki, T. Kamachi and M. Kohno, *Green Chem.*, 2016, **18**, 4536–4541.
29 D. K. Dinh, I. Muzammil, W. S. Kang, D. W. Kim and D. H. Lee, *Plasma Sources Sci. Technol.*, 2021, **30**, 055020.
30 T. Sakakura, S. Uemura, M. Hino, S. Kiyomatsu, Y. Takatsuji, R. Yamasaki, M. Morimoto and T. Haruyama, *Green Chem.*, 2018, **20**, 627–633.
31 P. Peng, P. Chen, M. Addy, Y. Cheng, Y. Zhang, E. Anderson, N. Zhou, C. Schiappacasse, R. Hatzenbeller, L. Fan, S. Liu, D. Chen, J. Liu, Y. Liu and R. Ruan, *Chem. Commun.*, 2018, **54**, 2886–2889.
32 J. Sun, T. Zhang, J. Hong, R. Zhou, H. Masood, R. Zhou, A. B. Murphy, K. K. Ostrikov, P. J. Cullen, E. C. Lovell, R. Amal and A. R. Jalili, *Chem. Eng. J.*, 2023, **469**, 143841.
33 P. Lamichhane, B. C. Adhikari, L. N. Nguyen, R. Paneru, B. Ghimire, S. Mumtaz, J. S. Lim, Y. J. Hong and E. H. Choi, *Plasma Sources Sci. Technol.*, 2020, **29**, 045026.
34 P. Heirman, W. Van Boxem and A. Bogaerts, *Phys. Chem. Chem. Phys.*, 2019, **21**, 12881–12894.
35 F. Judée, S. Simon, C. Bailly and T. Dufour, *Water Res.*, 2018, **15**(133), 47–59.
36 Y. Zhou, Y. Hong, Z. Li, Z. Bi, J. Zhang, J. Niu, J. Pan, J. Li and Y. Wu, *Vacuum*, 2019, **162**, 121–127.
37 A. Ozkan, T. Dufour, T. Silva, N. Britun, R. Snyders, A. Bogaerts and F. Reniers, *Plasma Sources Sci. Technol.*, 2016, **25**, 025013.
38 R. Li, Q. Tang, S. Yin and T. Sato, *Appl. Phys. Lett.*, 2007, **90**, 131502.
39 C. Wang, H. X. Wang, C. Y. Liu, X. Meng, G. Y. Jin, H. J. Huang, J. W. Cao, S. R. Sun and C. Yan, *Phys. Scr.*, 2023, **98**, 085605.
40 G. J. M. Hagelaar and L. C. Pitchford, *Plasma Sources Sci. Technol.*, 2005, **14**, 722.
41 S. Teodoru, Y. Kusano and A. Bogaerts, *Plasma Processes Polym.*, 2012, **9**, 652–689.
42 S. R. Sun, F. Chen, Y. H. Zheng, C. Wang and H. X. Wang, *Plasma Sources Sci. Technol.*, 2024, **33**, 075013.
43 A. Meiners, M. Leck and B. Abel, *Plasma Sources Sci. Technol.*, 2009, **18**, 045015.
44 N. Bolouki, W. H. Kuan, Y. Y. Huang and J. H. Hsieh, *Appl. Sci.*, 2021, **11**, 6158.
45 X. Tang, J. Wang, H. Yi, S. Zhao, F. Gao and C. Chu, *Plasma Chem. Plasma Process.*, 2018, **38**, 485–501.
46 P. Lukes, E. Dolezalova, I. Sisrova and M. Clupek, *Plasma Sources Sci. Technol.*, 2014, **23**, 015019.
47 G. Pierotti, C. Piferi, A. Popoli, M. Cavedon, A. Cristofolini, E. Martines and C. Riccardi, *Plasma Sources Sci. Technol.*, 2023, **32**, 064005.
48 J. T. Erron and D. S. Green, *Plasma Chem. Plasma Process.*, 2001, **21**, 459–481.
49 Y. Tang, J. Dai, P. Zhang, G. Niu, Y. Duan and Y. H. Tian, *ACS Sustainable Chem. Eng.*, 2024, **12**, 11319–11326.
50 R. Snoeckx, S. Heijkers, K. V. Wesenbeeck, S. Lenaerts and A. Bogaerts, *Energy Environ. Sci.*, 2016, **9**, 999–1011.
51 A. M. Lietz and M. J. Kushner, *J. Phys. D: Appl. Phys.*, 2016, **49**, 425204.
52 M. Gromov, N. Kamarinopoulou, N. D. Geyter, R. Morent, R. Snyders, D. Vlachos, P. Dimitrakellis and A. Nikiforov, *Green Chem.*, 2022, **24**, 9677–9689.
53 N. C. Roy, C. Pattyn, A. Remy, N. Maira and F. Reniers, *Plasma Processes Polym.*, 2021, **18**, 2000087.
54 Z. Ke, P. Thopan, G. Fridman, V. Miller, L. Yu, A. Fridman and Q. Huang, *Clin Plasma Med.*, 2017, **7**, 1–8.
55 S. M. Allabakshi, P. S. N. S. R. Srikar, S. Gomosta, R. K. Gangwar and S. M. Maliyekkal, *J. Hazard. Mater.*, 2023, **446**, 130639.
56 D. Mei, X. Zhu, C. Wu, B. Ashford, P. T. Williams and X. Tu, *Appl. Catal., B*, 2016, **182**, 525–532.
57 R. Khan, N. Rahman, A. Prasannan, K. Ganiyeva, S. Chakrabortty and S. Sangaraju, *Sci. Rep.*, 2025, **15**, 1–17.
58 H. Guo, N. Jiang, H. Wang, N. Lu, K. Shang, J. Li and Y. Wu, *J. Hazard. Mater.*, 2019, **371**, 666–676.
59 X. Pei, D. Gidon, Y. J. Yang, Z. Xiong and D. B. Graves, *Chem. Eng. J.*, 2019, **362**, 217–228.
60 B. S. Patil, N. Cherkasov, J. Lang, A. O. Ibhadon, V. Hessel and Q. Wang, *Appl. Catal., B*, 2016, **194**, 123–133.
61 Q. Sun, A. Zhu, X. Yang, J. Niu and Y. Xu, *Chem. Commun.*, 2003, **12**, 1418–1419.
62 A. A. Abdelaziz and H. H. Kim, *J. Phys. D: Appl. Phys.*, 2020, **53**, 114001.
63 M. Janda, V. Martišovitš, K. Hensel and Z. Machala, *Plasma Chem. Plasma Process.*, 2016, **36**, 767–781.
64 M. J. Pavlovich, T. Ono, C. Galleher, B. Curtis, D. S. Clark, Z. Machala and D. B. Graves, *J. Phys. D: Appl. Phys.*, 2014, **47**, 505202.
65 R. Hawtof, S. Ghosh, E. Guarr, C. Xu, R. M. Sankaran and J. N. Renner, *Sci. Adv.*, 2019, **5**, eaat5778.
66 W. Bian, J. Shi and X. Yin, *IEEE Trans. Plasma Sci.*, 2008, **37**, 211–218.
67 Y. S. Jin and C. Cho, *IEEE Trans. Plasma Sci.*, 2019, **47**, 4588–4592.
68 M. C. Wu, C. T. Liu, C. Y. Chiang, Y. J. Lin, Y. H. Lin, Y. W. Chang and J. S. Wu, *IEEE Trans. Plasma Sci.*, 2018, **47**, 1100–1104.
69 S. Islam, B. O. Farjana, S. A. Sajib, C. R. Nepal and A. Reza, *Gesunde Pflanz.*, 2019, **71**, 175–185.
70 M. Adhami, M. Narimisa, A. Nikiforov, M. Gromov, Y. Gorbanev, R. Bitar, R. Morent and N. D. Geyter, *Appl. Sci.*, 2023, **28**, 7619.
71 Y. Li, Q. Zhang, H. Dai, D. He, Z. Ke and X. Xiao, *Energy Environ. Sci.*, 2024, **17**, 9233–9243.